Navarro-Jiménez, J.; Navarro-García, H.; Tur Valiente, M.; Ródenas, JJ. (2020). Superconvergent patch recovery with constraints for three-dimensional contact problems within the Cartesian grid Finite Element Method. International Journal for Numerical Methods in Engineering. 121(6):1297-1313. https://doi.org/10.1002/nme.6266

Noname manuscript No.
(will be inserted by the editor)

Superconvergent patch recovery with constraints for 3D contact problems within the Cartesian grid Finite Element Method

José Manuel Navarro-Jiménez · Héctor Navarro-García · Manuel Tur · Juan José Ródenas

Received: date / Accepted: date

Abstract The Superconvergent Patch Recovery technique with constraints (SPR-C) consists in improving the accuracy of the recovered stresses obtained with the original SPR technique by considering known information about the exact solution, like the internal equilibrium equation, the compatibility equation or the Neumann boundary conditions, during the recovery process. In this paper the SPR-C is extended to consider the equilibrium around the contact area when solving contact problems with the Cartesian grid Finite Element Method (cgFEM). In the proposed method, the Finite Element stress fields of both bodies in contact are considered during the recovery process and the equilibrium is enforced by means of the continuity of tractions along the contact surface.

Keywords Superconvergent Patch Recovery · Contact · Cartesian grid · Immersed boundary

1 Introduction

The mechanical contact problem is present in several classical industrial applications such as tire-road, wheel-rail interactions, pin-on-disc wear or fretting. The contact problem is also being introduced in novel research areas like the patient specific study of the interaction between living tissue and prosthetic devices. We are interested in solving the contact between two linear elastic domains $\Omega^{(i)}$, $i = 1, 2$, considering a quasi-static approximation. The formulation of this problem can be written as follows:

J.M. Navarro-Jiménez · H. Navarro-García · M. Tur · J.J. Ródenas
Centro de Investigación en Ingeniería Mecánica, Departamento de Ingeniería Mecánica y de Materiales, Universitat Politécnica de Valencia, Camino de Vera s/n, 46022 Valencia, Spain
E-mail: jonaji@upv.es, hecnaga1@upv.es, manuel.tur@mcm.upv.es, jjrodena@mcm.upv.es

J.J. Ródenas
Healthcare Technology Group (GTS-IBV); Networking Biomedical Research Centre in Bioengineering, Biomaterials and Nanomedicine (CIBER-BBN), Valencia, Building 9C, Camino de Vera s/n, 46022 Valencia, Spain

$$
\begin{aligned}
&\operatorname{div} \boldsymbol{\sigma} + \mathbf{b} = 0 \\
&\boldsymbol{\sigma} = \mathbf{D}\boldsymbol{\varepsilon} \\
&\boldsymbol{\varepsilon} = \boldsymbol{\varepsilon}(\mathbf{u}) \\
&\mathbf{u}(\mathbf{x}) = \mathbf{u}_d(\mathbf{x}) \qquad \mathbf{x} \in \Gamma_D \\
&\mathbf{n} \cdot \boldsymbol{\sigma} = \hat{\mathbf{t}} \qquad \mathbf{x} \in \Gamma_N \\
&g_N \geq 0 \qquad \mathbf{x} \in \Gamma_C
\end{aligned}
\tag{1}
$$

where the displacements are represented by $\mathbf{u}$, the strain and stress tensors are $\boldsymbol{\varepsilon}, \boldsymbol{\sigma}$ respectively, $\mathbf{D}$ is the linear elasticity tensor and $\mathbf{b}$ denotes the volume forces. The boundaries of the analysis domains are divided in three non-overlapping regions $\{\Gamma_D, \Gamma_N, \Gamma_C\}$ where the Dirichlet, Neumann and contact constraints are imposed. The last constraint in (1) only accounts for the non-penetrability condition. Sliding contact can also be considered using frictional laws such as the Coulomb model [1].

The use of the Finite Element method to obtain an approximate solution of (1) has become a standard. In this framework the *a posteriori* error estimation of the approximate solution can be very useful in different aspects like error-driven mesh adaptation or error estimates in quantities of interest. A complete study of such methods can be found in [2]. The first developments in *a posteriori* error estimators for contact problems were in the context of node-to-node formulations. For example, an *h*-adaptive refinement strategy was guided by a residual based estimator in [3] and a stress recovery estimator in [4]. A posteriori errors have also been developed to guide *hp*-adaptive refinements in [5]. Since then, several error estimators have been proposed for contact problems involving non-matching meshes [6], using locally equilibrated fluxes [7] and mixed formulations [8], to cite a few.

Zienkiewicz and Zhu [9] proposed the ZZ error estimator for the disctretization error in energy norm, which is widely used within the FE community. The ZZ estimator can be formulated as:

$$
\|\mathbf{e}_{es}\| = \int_{\Omega} \left(\boldsymbol{\sigma}^* - \boldsymbol{\sigma}^h\right)^t \mathbf{D}^{-1} \left(\boldsymbol{\sigma}^* - \boldsymbol{\sigma}^h\right) \, d\Omega \tag{2}
$$

where Ω can be the whole analysis domain or a subdomain of it, $\boldsymbol{\sigma}^h$ is the FE stress field and $\boldsymbol{\sigma}^*$ is usually referred to as *smooth stress* or *recovered stress* field. Zienkiewicz and Zhu also developed a very efficient method to evaluate this field: the Superconvergent Patch Recovery [10], which is simple, robust and requires a considerably low computational cost. The ZZ estimator has been adapted to contact problems with different approaches. Some works in this direction are the use of the global version of the ZZ estimator for Coulomb's frictional contact [11] and its extension to multigrid methods in [12].

The Cartesian grid Finite Element Method (cgFEM) [13, 14] is an immersed boundary method developed for solving 2D [13] and 3D [14] elasticity problems. The main characteristic of the method is the use of approximation meshes with regular quadrilaterals (2D) or hexaedrons (3D) that are independent of the domain. The cgFEM features an efficient hierarchical data structure based on the use of nested Cartesian grids together with a special numerical integration procedure that enables one to capture the exact boundary definition through the use of NURBS. This method has been recently extended to solve 3D frictional contact problems [15] with a stabilized Lagrangian formulation in which the stabilization term is calculated with the SPR stress field. Moreover, the cgFEM features an *h*-adaptive refinement strategy based on the ZZ estimator and the SPR technique [16]. The accuracy of

the ZZ estimator relies directly on that of the smooth field $\boldsymbol{\sigma}^*$ [9]. Therefore, in this work we aim to improve the accuracy of the smooth field $\boldsymbol{\sigma}^*$ for contact problems to serve as stabilization stress and to efficiently guide the h-adaptive refinement.

Since the publication of the early SPR technique, several attempts to enhance the accuracy of the recovered field have been proposed. A thorough review of the different modifications of the SPR is presented in [17]. The same work proposes the SPR with constraints (SPR-C), which is based in the enforcement of known equilibrium equations of the 2D elasticity problem at a patch level. This work represents an extension of the SPR-C technique in which the contact constraint is weakly imposed for 3D elastic contact problems. The paper is structured as follows: section 2 features a brief review of the SPR and SPR-C methods, and some special features regarding the use of cgFEM are presented. In section 3 the contact condition constraint is included in the SPR-C. Finally, section 4 shows the performance of the technique with some numerical examples.

2 Superconvergent Patch Recovery with constraints: SPR-C

The idea behind the Superconvergent Patch Recovery [10] to compute the smooth field $\boldsymbol{\sigma}^*$ is the following: having a FE mesh, a recovery patch Ω_p^k is defined for each node k in the mesh, which is composed by all the elements containing the given node. Then, for each FE stress component σ_i^h, a polynomial field $\sigma_i^{*,k}(\mathbf{x}) = \mathbf{p}(\mathbf{x})\,\mathbf{a}_i^k$ is fitted to the values of σ_i^h at all Gaussian points $\mathbf{x}_g$ in the elements of Ω_p^k. The polynomial expansion $\mathbf{p}(\mathbf{x}) = \{1, x, y, z, ...\}$ is usually of the same degree as the FE approximation. The coefficients $\mathbf{a}_i^k \in \mathbb{R}^{N_k}$, where N_k is the dimension of vector $\mathbf{p}(\mathbf{x})$, are obtained solving a minimization problem:

$$\min_{\mathbf{a}_i^k \in \mathbb{R}^{N_k}} \frac{1}{2} \left[\sum_{g=1}^{N_g^k} \left(\mathbf{p}(\mathbf{x}_g)\,\mathbf{a}_i^k - \sigma_i^h(\mathbf{x}_g) \right)^2 \right] \tag{3}$$

where N_g^k stands the total number of Gaussian points $\mathbf{x}_g \in \Omega_p^k$. After solving all patches in the mesh, the smooth field $\boldsymbol{\sigma}^*$ can be computed at any point in the FE domain Ω^h by the same interpolation used in the FE approximation, with the nodal values $\sigma_i^{*,j}(\mathbf{x}_j)$ and the shape functions $N_j(\mathbf{x})$ associated to the j vertex nodes of element $\mathscr{E}$:

$$\sigma_i^*(\mathbf{x}) = \sum_j N_j(\mathbf{x}) \sigma_i^{*,j}(\mathbf{x}_j)\ ; \qquad \mathbf{x} \in \mathscr{E} \tag{4}$$

For elements with $p \geq 2$, the values at non-vertex nodes will, in general, be available from several patches and, following the advices presented in [18], $\sigma_i^{*,j}(\mathbf{x}_j)$ will be computed as an average of such values.

A straightforward idea to enhance the accuracy of $\boldsymbol{\sigma}^{*,k}$ consists in considering known information of the exact solution of the elasticity problem in equation (3). Following this idea, the Superconvergent Patch Recovery with constraints (SPR-C, [17]) is a modified version where the fulfillment of the internal equilibrium and Neumann boundary conditions are enforced at each patch by means of adding constraints to equation (3). As these equations involve the six components of the stress tensor $\{\sigma_1^{*,k}, ..., \sigma_6^{*,k}\}$ this version requires the simultaneous solution of all stress components. Therefore the smooth stress field is now defined with the block matrix $\mathbf{P}(\mathbf{x})$ and the column vector $\mathbf{A}^k$, which are written as:

$$\begin{aligned} &\boldsymbol{\sigma}^{*,k}(\mathbf{x}) = \mathbf{P}(\mathbf{x})\mathbf{A}^k \\ &\mathbf{P}(\mathbf{x}) = diag\left(\mathbf{p}(\mathbf{x}),...,\mathbf{p}(\mathbf{x})\right) \; ; \qquad \mathbf{A}^k = \left\{\mathbf{a}_1^k,...,\mathbf{a}_6^k\right\} \end{aligned} \tag{5}$$

Instead of the discrete approach of the standard SPR, an adaptation of the SPR-C technique to the X-FEM framework [19] considered a continuous formulation of the minimization problem (3). This approach provides better results for patches with different quadrature point densities in the elements, which is the case both in X-FEM and cgFEM [14], as the values at integration points are weighted [20]. Therefore, the modified minimization problem is the following:

$$\begin{aligned} &\min_{\mathbf{A}_i^k \in \mathbb{R}^{N_k \times 6}} \frac{1}{2}\left[\int_{\Omega_p^k}\left(\mathbf{P}(\mathbf{x})\mathbf{A}^k - \boldsymbol{\sigma}^h(\mathbf{x})\right)^2 d\Omega\right] \\ &\text{subject to } \mathbf{C}\mathbf{A}^k = \boldsymbol{\Lambda} \end{aligned} \tag{6}$$

where the additional constraints (to be defined later) have been included using a generic equation. Solving this problem by means of Lagrange Multipliers $\boldsymbol{\lambda}^k$, we obtain the following linear system of equations expressed in matrix form:

$$\begin{bmatrix} \mathbf{M} & \mathbf{C}^T \\ \mathbf{C} & \mathbf{0} \end{bmatrix} \begin{Bmatrix} \mathbf{A}^k \\ \boldsymbol{\lambda}^k \end{Bmatrix} = \begin{Bmatrix} \mathbf{H} \\ \boldsymbol{\Lambda} \end{Bmatrix} \tag{7}$$

where

$$\mathbf{M} = \int_{\Omega_p^k} \mathbf{P}(\mathbf{x})^T \mathbf{P}(\mathbf{x}) d\Omega \; ; \qquad \mathbf{H} = \int_{\Omega_p^k} \mathbf{P}(\mathbf{x})^T \boldsymbol{\sigma}^h(\mathbf{x}) d\Omega \tag{8}$$

A numerical integration scheme is used to evaluate the SPR coefficient matrix and vector defined in equation (8), using the integration quadratures built for the FE analysis.

Now the constraint equations are derived from the first and fifth equations in elasticity problem (1). Substituting equation (5) in the first equation of (1) we obtain the constraint equation to fulfill the **internal equilibrium**:

$$\nabla \cdot \mathbf{P}(\mathbf{x}) \; \mathbf{A}^k = -\mathbf{b}(\mathbf{x}) \; , \qquad \mathbf{x} \in \Omega_p^k \tag{9}$$

The SPR-C is also able to enforce the **Neumann boundary conditions** at patches containing any loaded or free boundary Γ_p^k. In this case the constraint equation is written as follows:

$$\mathbf{R}(\mathbf{x})\mathbf{P}(\mathbf{x}) \; \mathbf{A}^k - \mathbf{t}(\mathbf{x}) = \mathbf{0} \; , \qquad \mathbf{x} \in \Gamma_p^k \tag{10}$$

where $\mathbf{R}(\mathbf{x})$ is an operator that obtains the tractions vector from the stress components using the normal vector to the surface, and $\mathbf{t}(\mathbf{x})$ are the applied tractions ($\mathbf{t}(\mathbf{x}) = \mathbf{0}$ for free surfaces).

The contact constraint will be presented in section 3, and terms $\mathbf{C}$ and $\boldsymbol{\Lambda}$ in (7) will be detailed in section 2.1.3, where we will propose a method to weakly enforce the constraints (9) and (10).

The original version of the SPR consists in evaluating the stress polynomial at each node and then interpolating those values (equation (4)). To enhance the quality of this field,

Blacker and Belytschko proposed the *conjoint polynomials* technique [21], also used in [22]. In this method the smooth field is computed by the interpolation of the complete stress polynomial $\sigma_i^{*,j}(\mathbf{x})$ of the element's vertex nodes using the linear shape functions $N_j^v(\mathbf{x})$. Therefore, the smooth field is now written as:

$$\sigma_i^*(\mathbf{x}) = \sum_j N_j^v(\mathbf{x})\sigma_i^{*,j}(\mathbf{x}) \tag{11}$$

We will use this last definition in this work so we have re-used the same symbol σ_i^* from equation (4) to keep a simple notation.

Note that although obtaining local equilibrium in each patch, the process of interpolating a global smooth stress field introduces a lack of equilibrium of these constraints. As shown in ref. [22], if we evaluate the internal equilibrium for the smooth field $\boldsymbol{\sigma}^*$ taking into account equation (11) we obtain:

$$\nabla\cdot\boldsymbol{\sigma}^*(\mathbf{x}) = \sum_j \nabla\cdot N_j^v(\mathbf{x})\boldsymbol{\sigma}^{*,j} + \sum_j N_j^v(\mathbf{x})\nabla\cdot\boldsymbol{\sigma}^{*,j} \tag{12}$$

Considering the constraint in equation (9) and the partition of unity property of the shape functions, the second sum in equation (12) is equivalent to the volumetric forces $\mathbf{b}(\mathbf{x})$. Therefore the internal equilibrium of the smooth field results in:

$$\nabla\cdot\boldsymbol{\sigma}^*(\mathbf{x}) = \sum_j \nabla\cdot N_j^v(\mathbf{x})\boldsymbol{\sigma}^{*,j} + \nabla\cdot\mathbf{P}(\mathbf{x})\,\mathbf{A}^k = \sum_j \nabla\cdot N_j^v(\mathbf{x})\boldsymbol{\sigma}^{*,j} - \mathbf{b}(\mathbf{x}) \tag{13}$$

where the lack of equilibrium is due to the term $\sum_j \nabla\cdot N_j^v(\mathbf{x})\boldsymbol{\sigma}^{*,j} \neq 0$. Ref. [23] proved that this term can be used to obtain accurate asymptotic upper error bounds of the FE solution using recovery techniques. It is straightforward to obtain a similar term related to the Neumann boundary conditions in equation (10).

2.1 cgFEM 3D features regarding SPR-C

In the cgFEM the mesh is independent of the domain. Thus, there are some nodes outside the domain at the elements cut by the geometry (called boundary elements from now on) as well as elements completely inside the domain (internal elements). We can also distinguish between internal and boundary patches: internal patches contain only internal elements whereas boundary patches are those containing at least one boundary element. The internal equilibrium constraint will be enforced at both internal and boundary patches. Boundary patches cut by the Neumann boundary will also include the Neumann boundary conditions constraint. In this section we will detail the enforcement of such constraints and show some features that improve the efficiency of the SPR technique within the cgFEM.

2.1.1 Boundary patch enlargement

The arbitrary intersection between the Cartesian grids and the analysis domain may produce some elements with a low volume of material inside, as in the example shown in Figure 1a. In that case the stiffness associated to the external node colored in red becomes very small, which results in an ill-conditioning of the FE formulation [24] and also a poor quality of the FE stress field computed at those *pathological* elements. In the classical SPR procedure

the patch Ω_p^k associated to the red node in Figure 1a would consist only in that pathological element. Then, the smooth field $\boldsymbol{\sigma}^*$ would eventually have a lower quality in that region. To avoid these situations we measure the ratio between material and element volume for each boundary patch (all internal patches will have a 100% ratio). If the patch volume ratio is under a certain threshold, the patch is enlarged by including the adjacent elements, as shown in Figure 1b. All the tests in this paper were carried out with a threshold value of 25%, with acceptable results.

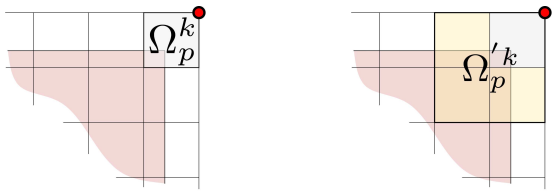

(a) Original patch (b) Enlarged patch

Fig. 1: Example of boundary patch enlargement. The patch Ω_p^k associated to the red node has a low material/element volume ratio. Hence a bigger patch $\Omega_p^{'k}$ that also includes the surrounding elements is considered.

2.1.2 Patch coding

In order to reduce ill-conditioning problems when solving equation (7) a normalized local coordinate system centred at the patch node is used instead [25]. Therefore, for a given node with coordinates $\mathbf{x}_N$, the local coordinate system built for its recovery patch is defined as:

$$\mathbf{x}_{local} = \frac{\mathbf{x} - \mathbf{x}_N}{h_p} \tag{14}$$

where h_p is a representative size of the patch, e.g. the biggest element size in the patch. Taking into account this variable change, the coefficient matrix $\mathbf{M}$ in (7) only depends on the relative position of the integration points inside the patch. This implies that patches with the same shape will share the coefficient matrix, and only one matrix inversion for each different patch topology is needed to calculate the SPR coefficients.

In cgFEM h-adapted meshes only one level difference is allowed between adjacent elements. Hence, since all the elements in the cgFEM are quadrilaterals/hexahedrons there is a finite number of internal patch topologies. Figure 2a shows all possible patch configurations that exist in a 2D cgFEM mesh.

However, there are still hundreds of possible patch topologies in a cgFEM 3D mesh (some examples are shown in Figure 2b). Instead of manually coding all the configurations we have designed an efficient automatic coding of the patches based on the relative size of the elements within the patch. Then, given a FE mesh, all internal patch topologies in the mesh are detected, and the coefficient matrix $\mathbf{M}$ is evaluated and inverted once only for the present topologies. Figure 3 shows an example of the automatic coding for 2D patches. The bigger element in the patch is defined as level 0 and smaller elements have increasing values.

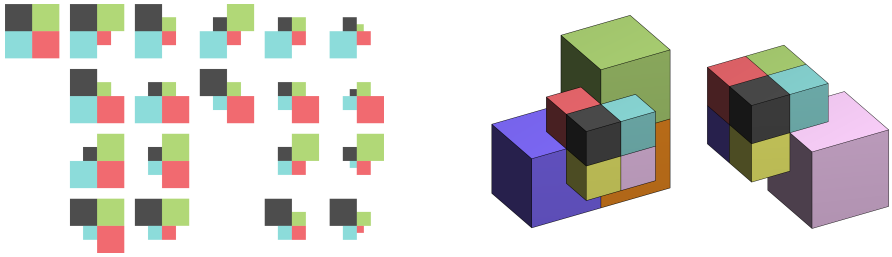

(a) (b)

Fig. 2: Patch topologies that can appear in a cgFEM analysis. All 19 possible configurations for cgFEM 2D (a), and examples of possible configurations for cgFEM 3D (b).

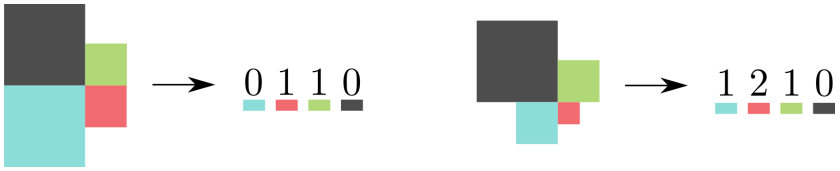

Fig. 3: 2D example of SPR patch coding. The patch on the left has code number 0110 and the patch on the right is number 1210.

A decimal number for the patch topology is obtained by concatenating all levels in the patch (4 digits for 2D patches, 8 digits for 3D patches).

Despite not being compact, this system avoids manual classification and coding of all possible 3D patches that may exist in a cgFEM 3D analysis. With this procedure the computational cost of the recovery process for the internal patches can be neglected if compared with the evaluation at boundary patches, as these must be solved individually. This could be seen as a $(d-1)$-dimensional computational cost associated to the recovery procedure.

2.1.3 SPR-C constraints enforcement

The recovered field $\boldsymbol{\sigma}^*$ cannot satisfy the enforced equilibrium equations for all points in the domain (or boundary) in the general case. For instance, if $\boldsymbol{\sigma}^*$ is a polynomial of degree 2 the internal equilibrium equation (9) is only fulfilled for linear volumetric forces $\mathbf{b}(\mathbf{x})$. Similarly, it is not possible to strongly enforce the Neumann boundary conditions for generic tractions and/or curved boundaries. A possible alternative is the strong enforcement of the constraint equations at a set of points in the patch to provide a number of linearly independent equations equal to the number of constraints. However, the location of such points in 3D results to be arbitrary and cumbersome.

We propose the weak enforcement of the equilibrium constraints using a pseudoinverse approach. For the case of the internal equilibrium, equation (9) is now written as the following numerical integration, where the subscript g denotes each quadrature point $\mathbf{x}_g \in \Omega_p^k$ with quadrature weight w_g:

$$\sum_{g=1}^{N_g^k} \nabla \cdot \mathbf{P}(\mathbf{x}_g) w_g \mathbf{A}^k = -\sum_{g=1}^{N_g^k} \mathbf{b}(\mathbf{x}_g) w_g \tag{15}$$

Matrix $\mathbf{C}^{iee}$ and a vector $\boldsymbol{\Lambda}^{iee}$ are built such that each row represents the enforced constraint (15), that is:

$$\begin{aligned} &\mathbf{C}_g^{iee}\mathbf{A}^k = \boldsymbol{\Lambda}_g^{iee} \quad \forall \mathbf{x}_g \in \Omega_p^k \\ &\mathbf{C}_g^{iee} = \nabla\cdot\mathbf{P}(\mathbf{x}_g)w_g\ ; \qquad \boldsymbol{\Lambda}_g^{iee} = -\mathbf{b}(\mathbf{x}_g)w_g \end{aligned} \tag{16}$$

Then the set of linearly independent columns $\mathbf{C}^{*iee}$ is selected from the constraint matrix, and the constraint block of equations included in problem (6) is:

$$\mathbf{C}^{*iee'}\mathbf{C}^{iee}\mathbf{A}^k = \mathbf{C}^{*iee'}\boldsymbol{\Lambda}^{iee} \tag{17}$$

This generic approach is applied independently for any type of constraint included in problem (6), so, for the Neumann boundary conditions, we will write equation (10) at each quadrature point as:

$$\begin{aligned} &\mathbf{C}_g^{ext}\mathbf{A}^k = \boldsymbol{\Lambda}_g^{ext} \quad \forall \mathbf{x}_g \in \Gamma_p^k \\ &\mathbf{C}_g^{ext} = \mathbf{R}(\mathbf{x}_g)\mathbf{P}(\mathbf{x}_g)w_g\ ; \qquad \boldsymbol{\Lambda}_g^{ext} = -\mathbf{t}(\mathbf{x}_g)w_g \end{aligned} \tag{18}$$

and then a procedure similar to (17) is applied. The resulting blocks of constraint equations are concatenated to form $\mathbf{C}$ and $\boldsymbol{\Lambda}$ in the system (7). For example, a boundary patch that contains a loaded surface will have the following blocks of constraint equations:

$$\mathbf{C} = \begin{Bmatrix} \mathbf{C}^{*iee'}\mathbf{C}^{iee} \\ \mathbf{C}^{*ext'}\mathbf{C}^{ext} \end{Bmatrix}\ ; \qquad \boldsymbol{\Lambda} = \begin{Bmatrix} \mathbf{C}^{*iee'}\boldsymbol{\Lambda}^{iee} \\ \mathbf{C}^{*ext'}\boldsymbol{\Lambda}^{ext} \end{Bmatrix} \tag{19}$$

3 Contact condition constraint

Consider two elastic bodies $\Omega^{(1)}$ and $\Omega^{(2)}$ in contact, and let $\Gamma_C^{(i)},\ i=1,2$ be the part of the boundary that is likely to become in contact. When both solids are in equilibrium the deformed boundary $\Gamma_C^{(i)_d}$ will comprise all point pairs from both bodies that have an active contact condition. Similarly to the ideas presented in the SPR-C, we would like to enforce the equilibrium along the contact boundary. Since two different stress fields take part in $\Gamma_C^{(i)_d}$ (one belonging to each body in contact), the stress distribution corresponding to the exact solution should fulfill the following equilibrium equation:

$$\mathbf{t}^{(1)}(\mathbf{x}) + \mathbf{t}^{(2)}(\mathbf{x}) = \mathbf{0} \tag{20}$$

It is worth to remark that this constraint equation is valid for both frictionless and frictional contact models, since we only enforce the continuity of the traction vector between bodies. Similarly to the Neumann boundary conditions, $\mathbf{t}^{(i)}(\mathbf{x})$ are given by

$$\mathbf{R}^{(i)}(\mathbf{x})\mathbf{P}^{(i)}(\mathbf{x})\ \mathbf{A}^{(i)} = \mathbf{t}^{(i)}(\mathbf{x})\ , \qquad \forall \mathbf{x} \in \Gamma_C^{(i)_d}\ , \qquad i=1,2 \tag{21}$$

therefore we can rewrite the equilibrium equation at the contact boundary as:

$$\mathbf{R}^{(1)}(\mathbf{x})\mathbf{P}^{(1)}(\mathbf{x})\ \mathbf{A}^{(1)} + \mathbf{R}^{(2)}(\mathbf{x})\mathbf{P}^{(2)}(\mathbf{x})\ \mathbf{A}^{(2)} = \mathbf{0} \tag{22}$$

Note that the coefficients $\mathbf{A}^{(i)}$ of the SPR are defined at nodes of each FE mesh. However, the cgFEM deals with non-conforming meshes, and the association between nodes of both bodies in contact is unclear. Our approach is the following: we define a *main* body where the SPR-C will be performed (e.g $\Omega^{(1)}$), and the *auxiliary* body in contact (e.g. $\Omega^{(2)}$). We

associate a region of the auxiliary body Ω^k_{aux} to each patch Ω^k_p at the main body with active contact points. Then we define another SPR-C problem at Ω^k_{aux} with the unknown coefficients $\mathbf{A}^{*(2)}$ and couple both problems with equation (22). Finally the system of equations that will be solved for a patch at the main body is an expansion of equation (7):

$$\begin{bmatrix} \mathbf{M}^{(1)} & \mathbf{0} & \mathbf{C}^{(1)T} & \mathbf{0} & \mathbf{C}^{cont\,T} \\ \mathbf{0} & \mathbf{M}^{(2)} & \mathbf{0} & \mathbf{C}^{(2)T} & \\ \mathbf{C}^{(1)} & \mathbf{0} & & & \\ \mathbf{0} & \mathbf{C}^{(2)} & & \mathbf{0} & \\ \mathbf{C}^{cont} & & & & \end{bmatrix} \begin{Bmatrix} \mathbf{A}^{(1)} \\ \mathbf{A}^{*(2)} \\ \boldsymbol{\lambda}^{(1)} \\ \boldsymbol{\lambda}^{(2)} \\ \boldsymbol{\lambda}^{cont} \end{Bmatrix} = \begin{Bmatrix} \mathbf{H}^{(1)} \\ \mathbf{H}^{(2)} \\ \boldsymbol{\Lambda}^{(1)} \\ \boldsymbol{\Lambda}^{(2)} \\ \mathbf{0} \end{Bmatrix} \tag{23}$$

where the blocks in red correspond to the stress field in the main body, the green blocks correspond to the stress field in the auxiliary domain, and the contact constraint $\mathbf{C}^{cont}$ which enforces the continuity of both fields over the contact interface is derived from equation (22) as:

$$\mathbf{C}^{cont} = \left[\mathbf{R}^{(1)}(\mathbf{x})\mathbf{P}^{(1)}(\mathbf{x}) \,, \quad \mathbf{R}^{(2)}(\mathbf{x})\mathbf{P}^{(2)}(\mathbf{x}) \right] \tag{24}$$

As the problem considered for the auxiliary body is not associated with a particular node of its mesh, the coefficients $\mathbf{A}^{*(2)}$ cannot be used to create a recovered stress field. Therefore the solution of (23) provides two sets of coefficients, $\mathbf{A}^{(1)}$ and $\mathbf{A}^{*(2)}$, but only those regarding the *main* body can be considered for the evaluation of the smooth stress field. An analogous procedure exchanging the *main* and *auxiliary* roles is followed to obtain the coefficients $\mathbf{A}^{(2)}$. With these considerations the recovered stress fields will not exactly fulfill equation (22) at a patch level, which we find assumable since the calculation of the smooth stress $\boldsymbol{\sigma}^*$ already introduces a lack of equilibrium (shown in section 2).

Now we need to define Ω^k_{aux} for each patch of the *main* body. There are many possibilities to achieve this goal. In this work we have decided to split the procedure in two stages: a) selection of a region in the *auxiliary* body, $\Omega^{\mathscr{E}}_{aux}$, associated to each element $\mathscr{E}$ in the *main* body cut by the contact area, and b) creation of an auxiliary region Ω^k_{aux} for each patch Ω^k_p containing, at least, one of these elements. Here below we present the steps followed to assign an auxiliary region $\Omega^{\mathscr{E}}_{aux}$ to each element $\mathscr{E}$. In this description we use the indices i and j to represent the *main* and *auxiliary* bodies, respectively.

1. We identify the set of contact points $P^{\mathscr{E}}_{\Gamma^{(i)}}$ within the element $\mathscr{E}$. Taking only the points with an active contact condition into account, $P^{\mathscr{E}}_{\Gamma^{(i)}}$ will contain: a) quadrature points of the slave surface, if the *main* body is the slave body; b) projections of these points on the master surface, if the *main* body is the master body, or c) both of them, if an unbiased formulation (*double pass*) is considered. An additional set $S^{\mathscr{E}}_{\Gamma^{(i)}}$ will be used. This is the union of $P^{\mathscr{E}}_{\Gamma^{(i)}}$ and the intersections between the element edges with the active section of the contact surface. For example, $S^{\mathscr{E}}_{\Gamma^{(i)}}$ is depicted by all the green entities in Figure 4a.
2. We compute an average point $\mathbf{x}_c$ and an average unit normal vector $\mathbf{n}_c$ of $\Gamma_C \cap \mathscr{E}$ as the weighted arithmetic mean of the coordinates $\mathbf{x}_a$ and normal vectors to the surface $\mathbf{n}_b$ associated to the contact points $P^{\mathscr{E}}_{\Gamma^{(i)}}$. The weighting values are those of the surface numerical integration.
3. We use $\mathbf{x}_c$ and $\mathbf{n}_c$ to define the plane Ψ, which is perpendicular to $\mathbf{n}_c$ and contains $\mathbf{x}_c$, as shown in Figure 4b.

4. We build the set $\widetilde{\mathscr{P}}^{(j)}$ which groups the elements in the *auxiliary* body mesh $\mathscr{P}^{(j)}$ that contain the pairs of the points in $S^{\mathscr{E}}_{\Gamma^{(i)}}$. Then $P^{\mathscr{E}}_{\Omega^{(j)}}$ is defined as the set containing all volume integration points in $\widetilde{\mathscr{P}}^{(j)}$. This step is depicted in Figure 4c.
5. We obtain $\boldsymbol{\eta}_a = \boldsymbol{\Phi}(\mathbf{x}_a)$ and $\boldsymbol{\eta}_b = \boldsymbol{\Phi}(\mathbf{x}_b)$ by orthogonally projecting the points $\mathbf{x}_a \in S^{\mathscr{E}}_{\Gamma^{(j)}}$ and $\mathbf{x}_b \in P^{\mathscr{E}}_{\Omega^{(j)}}$ onto the plane Ψ, with $\boldsymbol{\Phi}$ being to the mapping operator. This transformation is shown in Figure 4d.
6. The contact region $\overline{S}^{\mathscr{E}}_{\Gamma^{(i)}}$ is then approximated by the convex hull of $\boldsymbol{\eta}_a$ (the yellow shapes in Figure 4d).
7. Finally, the auxiliary region $\Omega^{\mathscr{E}}_{aux}$ is defined as the subset of points in $P^{\mathscr{E}}_{\Omega^{(j)}}$ whose projections $\boldsymbol{\eta}_b$ are inside $\overline{S}^{\mathscr{E}}_{\Gamma^{(i)}}$ (Figures 4e and 4f).

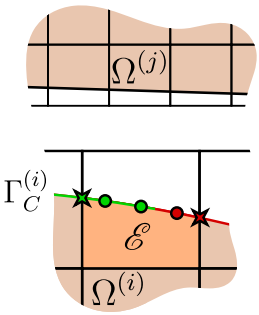

(a) Element $\mathscr{E}$ with active contact condition. The contact area is depicted in green. The integration and intersection points are presented as circles and stars respectively.

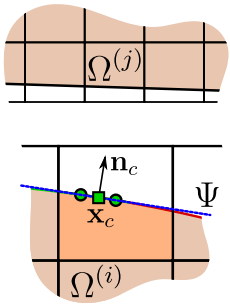

(b) Definition of the plain Ψ associated to the contact area.

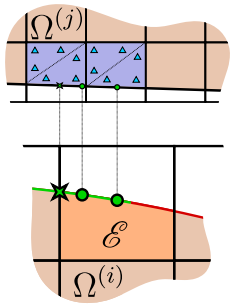

(c) Volume integration points in the *auxiliary* body that may be contained in the auxiliary domain.

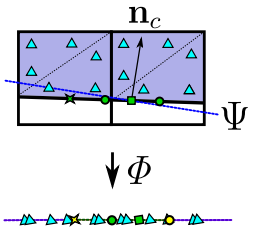

(d) Proyection of the points of interest onto the plane Ψ. The space between the yellow points is the contact region $\overline{S}^{\mathscr{E}}_{\Gamma^{(i)}}$.

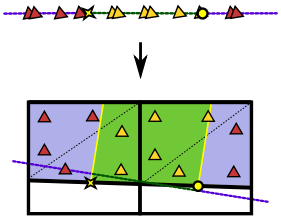

(e) Classification of volume points. The yellow triangles represent the points selected to create $\Omega^{\mathscr{E}}_{aux}$.

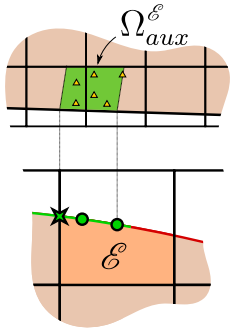

(f) Auxiliary domain associated to the element $\mathscr{E}$

Fig. 4: Definition of the auxiliary domain $\Omega^{\mathscr{E}}_{aux}$ at element level for the solution of the SPR-C problem at patches with contact points.

In the second stage, the auxiliary domain Ω^k_{aux} of the patch Ω^k_p is constructed as the union of the auxiliary domains of the elements in the patch: $\Omega^k_{aux} = \{\Omega^{\mathscr{E}}_{aux} | \mathscr{E} \subset \Omega^k_p\}$. This is illustrated in Figure 5.

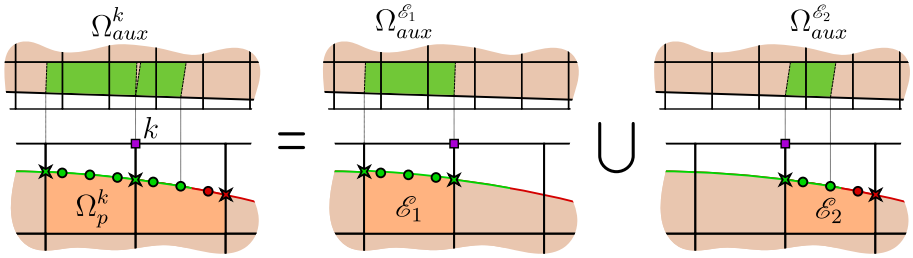

Fig. 5: Creation of the auxiliary region Ω^k_{aux} from those computed at element level

4 Numerical examples

In this section three contact problems are solved to test the proposed recovery procedure. The quality of the presented SPR-C with contact constraints is evaluated with respect to several goals, namely the enforcement of the tractions between the two bodies in contact, the effectivity of the error estimator and the suitability for *h*-adaptive refinement. We have used a stabilized Lagrangian formulation [15], which is suitable for both frictionless and friction contact, for the solution of the problems presented in this section.

4.1 Example 1. Contact test between elastic solids

An analysis of the differences between the recovered field calculation with and without contact constraints is performed in the following problem involving two elastic solids in contact. A 2D sketch of the problem is shown in Figure 6 left. At the initial configuration both contact surfaces are overlapping (there is no such space between solids), and a vertical displacement $d = -1.6 \cdot 10^{-6}$ m is applied on the upper face of body 2. Symmetry conditions are applied on the faces parallel to the yz plane, and displacements along y direction are constrained at a point to avoid rigid body motions. Two lateral faces of body 1 are loaded with $p_y = 4 \cdot 10^{11}(0.01 - z)z$ Pa and $p_z = 10 \cdot 10^{11}(0.01 - z)z$ Pa. The material properties, identical for both solids, are $E = 115$ GPa and $\nu = 0.3$. Three non-conforming uniformly *h*-refined meshes were solved in the analysis (Figure 6), using the standard recovery technique (SPR) and the constrained version including contact constraints (SPR-C). We also considered a reference solution coming from a 2D overkilled mesh analysis.

The contact pressure $p_N = \mathbf{n} \cdot \boldsymbol{\sigma}^* \cdot \mathbf{n}$ evaluated at a path along y direction is shown in Figure 7a for the upper solid. An improvement of the recovered field can be appreciated in two different aspects. First, the maximum contact pressure estimation is much closer to the reference values. Furthermore, the enforcement of Neumann boundary conditions also ensures null tractions over non-contact regions. The results show that both effects have a higher impact on the recovered field as the mesh is coarser.

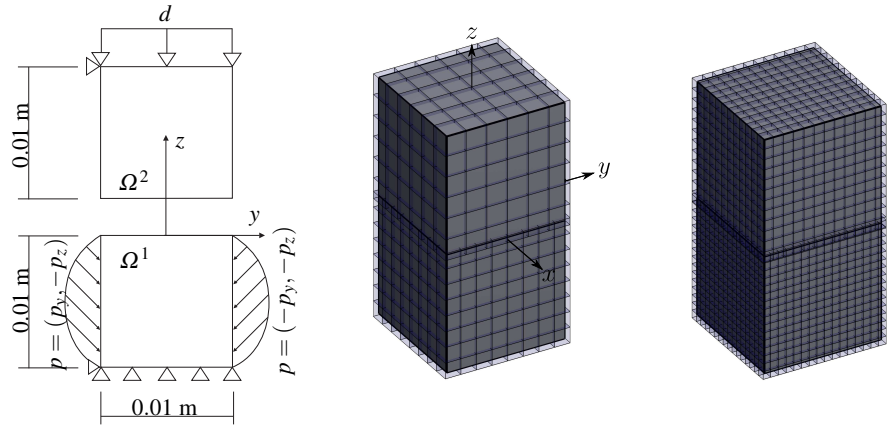

Fig. 6: Example 1. Sketch of the problem and two analysis meshes. A third mesh obtained by dividing the right-most mesh was also used in the analysis.

As a consequence of these improvements, it might be seen that there is a better estimation of the end-of-contact area. However, is not possible to provide with accurate estimates of the end-of-contact point (line in 3D) using regular polynomials for the recovered stress field given the regularity of the exact solution. Although there is a considerably enhanced estimation of the stress gradient, the location of this area is still highly influenced by the mesh. This is illustrated with the results shown in Figure 7b. The contact pressure is evaluated at both bodies and the difference is normalized with respect to the maximum contact pressure obtained at the reference solution (9.49 MPa). The vertical discontinuous lines represent the end-of-contact points for the reference solution. Note that the addition of contact constraints in the SPR-C results in a considerably lower lack of equilibrium inside the contact area. However, there is no such improvement in the end-of-contact area. As the analysis meshes are non-conforming the recovery process estimates these areas at a different location for each body, thus locally increasing the lack of equilibrium. The results also show that this local error is alleviated with the mesh *h*-refinement.

Note that the ZZ-estimator (2) becomes the exact error in energy norm $\|\mathbf{e}_{ex}\|$ if the considered problem had an analytical solution (which is usually not available). In that case, we can define the effectivity index Θ of the error estimator as $\Theta = \|\mathbf{e}_{es}\| \,/\, \|\mathbf{e}_{ex}\|$. A good error estimator should converge to $\Theta = 1$ as the mesh is refined. Figure 8 shows the effectivity of the ZZ-estimator in this problem using the standard SPR and the proposed SPR-C, assuming the overkilled solution as reference. Although the error estimator is evaluated at all the domain there is a substantial improvement in the effectivity values, especially for coarse meshes. In order to evaluate the local improvement of the estimator around the contact area, the integrand of equation (2) is evaluated at the quadrature points on the contact surface of the lower body calculating the smooth field $\boldsymbol{\sigma}^*$ with SPR, SPR-C and the reference solution. This comparison allows to qualitatively evaluate the accuracy of the recovered field on the contact area. Results show that the SPR-C estimator detects error due to the end-of-contact and free surface areas, whereas the SPR based estimator is not able to capture those errors. It can also be seen that the error in the end-of-contact area is underestimated by the SPR-C.

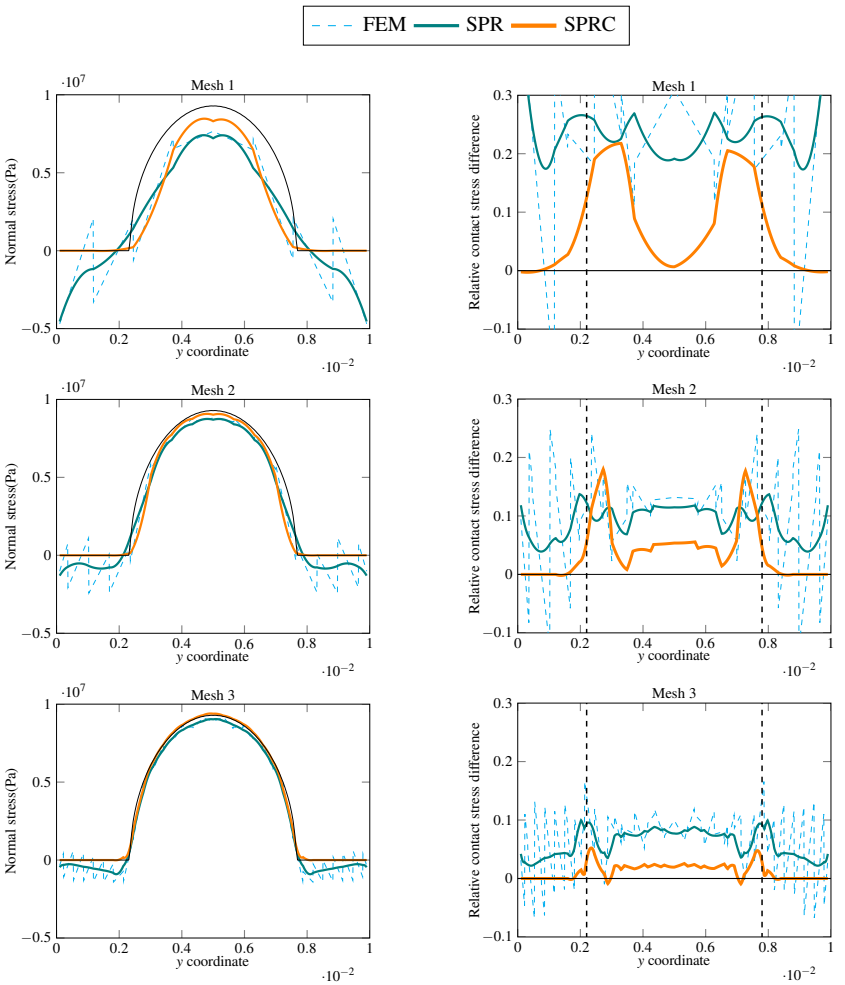

(a) Distribution of the normal stress evaluated at the upper body. Positive values of the stress stand for compression.

(b) Contact stress difference between the two bodies ($\sigma^2\mathbf{n}^2 - \sigma^1\mathbf{n}^1$). Values are normalized with the reference maximum contact stress. The contact area lies between the vertical discontinuous lines.

Fig. 7: Example 1. Evolution of the different magnitudes along a path that follows the y direction

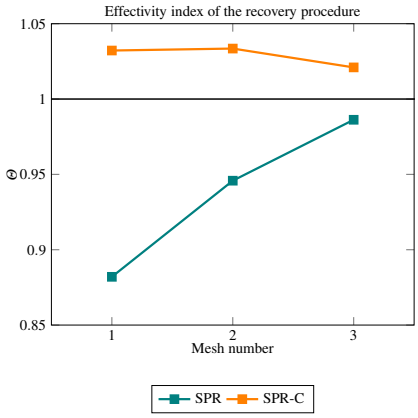

Fig. 8: Example 1. Effectivity of the error estimation using SPR and SPR-C taking the overkilled mesh solution as reference.

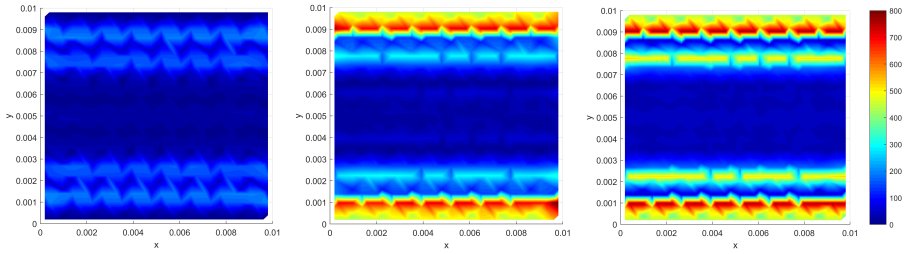

(a) $\boldsymbol{\sigma}^*_{SPR} - \boldsymbol{\sigma}^h$ (b) $\boldsymbol{\sigma}^*_{SPR-C} - \boldsymbol{\sigma}^h$ (c) $\boldsymbol{\sigma} - \boldsymbol{\sigma}^h$

Fig. 9: Example 1. Evaluation of the error estimation integrand $\left(\boldsymbol{\sigma}^* - \boldsymbol{\sigma}^h\right)\mathbf{D}^{-1}\left(\boldsymbol{\sigma}^* - \boldsymbol{\sigma}^h\right)$ over the contact surface at the lower body using different stress fields. Results correspond to the first analysis mesh.

4.2 Example 2. Cylinder-plane contact

The second example simulates the contact between a block with cylindrical surface and a parallelepiped. The geometric model of the problem is depicted in Figure 10a, with the dimensions $L = 4$ mm and $R = 50$ mm. A linear elastic material is used for both bodies with properties $E = 115$ GPa and $\nu = 0.32$. A vertical displacement $d = -1.77x10^{-5}$ m is applied on the upper face of the cylindric body and vertical displacements are constrained on the lower face of the parallelepiped.

Symmetry conditions are applied on the surfaces perpendicular to the z axis and rigid body motions are properly constrained along x. Both bodies are initially meshed with non-conforming uniform grids of size $h \approx 0.5$ mm as shown in Figure 10b. Two different analysis are compared in this example. First a sequence of three uniformly h-refined meshes is solved, with the finest mesh containing 135045 degrees of freedom. In the second test an automatic h-adaptive refinement procedure based on the ZZ-error estimator is used [26], and the SPR-C presented in this work is used to obtain the smooth stress field. Figure 11 shows the

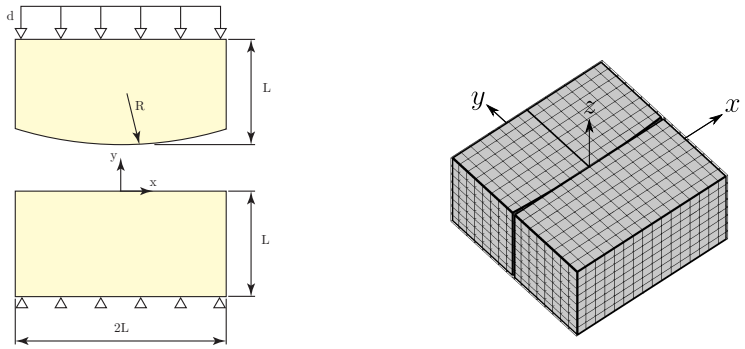

(a) (b)

Fig. 10: Example 2. (a) Geometry model for the cylinder-plane contact problem. (b) Initial analysis mesh, containing 8262 degrees of freedom.

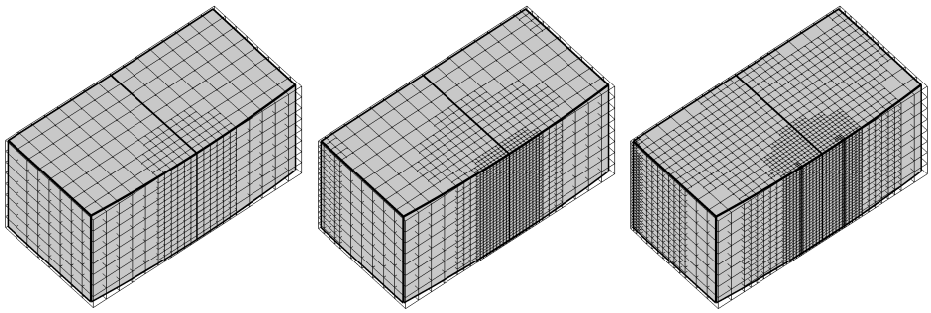

(a) 15468 DOF (b) 46140 DOF (c) 135045 DOF

Fig. 11: Example 2. Sequence of three meshes obtained through error-based *h*-adaptive refinement. Detail of body 2. For each mesh the DOF number of the complete problem is shown.

sequence of meshes obtained with this procedure for the cylindrical body. Similar meshes are obtained on the other body in the analysis. It is worth noting that the refinement algorithm automatically adapts the mesh around the end-of-contact area, where the highest gradient of the solution arises. A 2D overkilled solution has been solved again to serve as a reference and compare the error of both strategies (Figure 12). Two conclusions can be extracted from these results: first, the optimal convergence rate is obtained for the uniform refinement analysis; and secondly, the automatic adaptive refinement strategy is more efficient in the sense that it can provide the same accurate results with approximately a quarter of the DOFs in this particular problem.

Finally, the effectivity of the ZZ-error estimator is compared again between the use of SPR and SPR-C. The effectivity index Θ presented in the previous example can also be calculated element-by-element to locally assess the quality of the estimator. However, this index does not provide clear representations of the recovery performance because the values are not balanced, that is, "underestimation" efficiencies range between $(0, 1)$ and

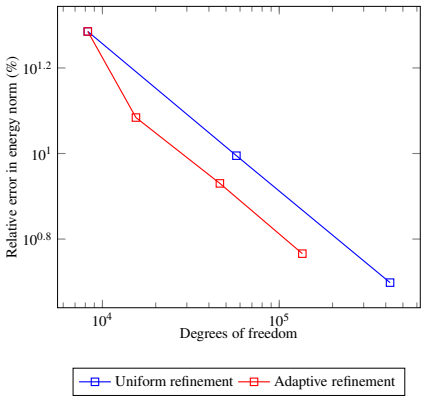

Fig. 12: Example 2. Comparison of the error in energy norm with uniform and adaptive *h*-refinement using SPR-C in the ZZ-estimator.

"overestimation" efficiencies are in the $(1,+\infty)$ range. To overcome this issue, the *local effectivity* index is defined as:

$$\begin{cases} D = 1 - \dfrac{1}{\Theta}; & 0 < \Theta < 1 \\ D = \Theta - 1\,; & \Theta \geq 1 \end{cases} \tag{25}$$

This definition of the local effectividy index, inspired by the robustness index described by Babuska et al. [27], is appropriate as it produces values in $(-\infty,0)$ for error underestimates of the error and in $(0,+\infty)$ when the error is overestimated. Using the last mesh of the adaptive refinement sequence we have compared the accuracy of the SPR and SPR-C by means of the local effectivity index D. This index is evaluated in Figure 13 at the elements cut by the cylinder surface, where we can distinguish the contact area where the elements are more refined. In the color map a red color denotes overestimation of the error and blue colors indicate underestimation of the error. It is clearly seen that the SPR without constraints underestimates the error around the end-of-contact area, whereas the SPR-C has an overall better performance on the contact area. It is also worth to remark that the performance of the estimator is considerably deteriorated far from the contact zone because the discretization is coarser.

4.3 Example 3. Frictional contact between curved surfaces

In the final example a frictional contact problem involving curved surfaces is solved. Both solids have a toroidal shape with identical geometry parameters, major and minor radius of $R = 1.5$ cm and $r = 0.5$ cm respectively. The initial configuration of the problem is shown in Figure 14a, where the blue colored surfaces are clamped and a constant displacement along y direction of 0.05 cm is applied on the orange colored surfaces. The problem is solved considering a Coulomb frictional model with a friction coefficient of $\mu = 1$ and linear elastic material with $E = 115$ GPa, $\nu = 0.3$. We have conducted again two different *h*-refinement strategies in this example, the uniform and the automatic adaptive using the ZZ-error estimator and the SPR-C smoothed stress. The error estimation results, presented in Figure 15, show that the FE convergence rate is kept once again for the uniform refinement

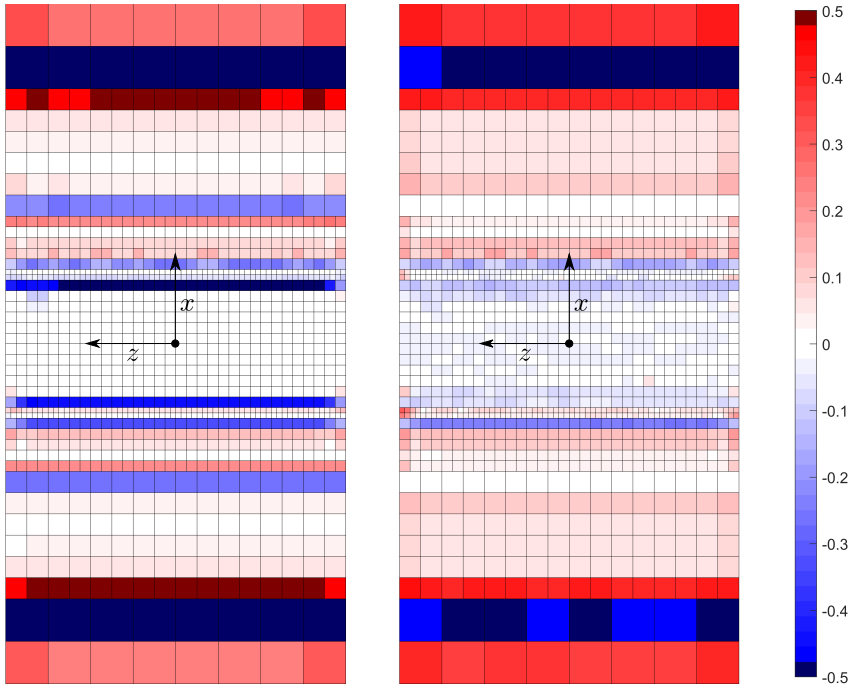

(a) (b)

Fig. 13: Example 2. Color map of the local effectivity D evaluated at the contact surface for the finest h-adapted mesh using SPR (a) and SPR-C (b).

and that the adaptive strategy is more efficient in terms of computational cost for a prescribed error.

Figure 16 shows a detail around the contact area in one of the bodies for all the discretization meshes in the refinement sequence. In order to highlight the discretization of the surface, only the intersection cuts between the Cartesian grid and the surface are shown. Note that the mesh is again automatically refined around the contact area, which in this case has a circular shape. The contact area can be distinguished in Figure 16, which represents the values of the normal component of the surface tractions, $(\mathbf{n}\cdot\boldsymbol{\sigma})\mathbf{n}$, using the FE stress field and the smooth stress obtained with the SPR-C. The negative values represent compression stress, and the color map has been modified so that positive values of normal traction, which are physically unfeasible since the surfaces are not loaded, are represented in black. It can be seen that besides smoothing the FE stress field, which is discontinuous, the positive tractions are removed on the recovered solution thanks to the additional constraints of the SPR-C.

5 Conclusions

We have presented a modified version of the Superconvergent Patch Recovery with constraints (SPR-C) that includes the traction equilibrium at the contact area for frictionless and friction problems. For each patch containing active contact points, an auxiliary SPR problem with information of both contacting bodies is used. The constraints are enforced in a

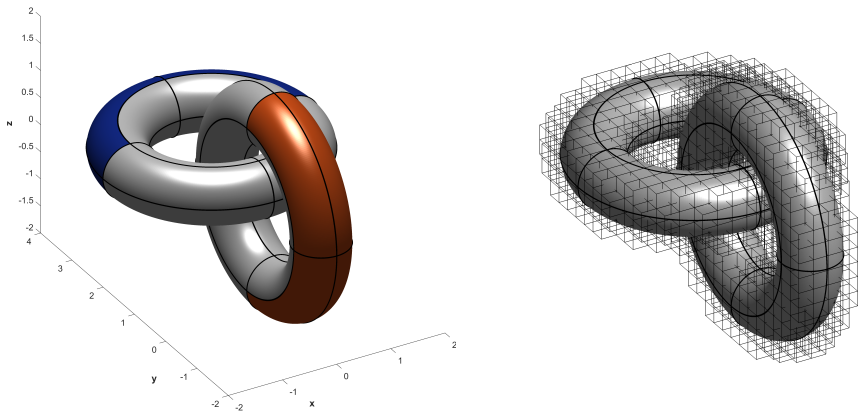

(a) Problem scheme (b) Analysis mesh

Fig. 14: Example 3. Model of the contact problem between curved solids. Lengths in cm. Surfaces in blue are clamped, and a constant displacement $u_y = -0.05$ cm is applied on the orange surfaces. The initial mesh is a non-conforming uniform grid with element size of $h \approx 0.25$ cm for both bodies.

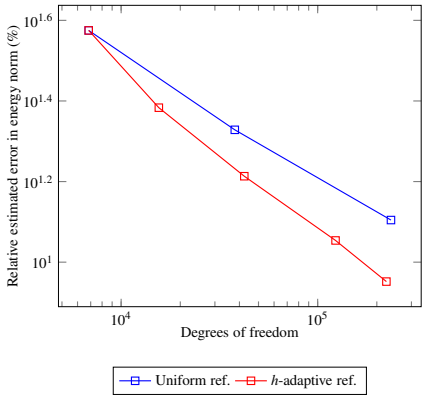

Fig. 15: Example 3. Comparison of the error in energy norm with uniform and adaptive h-refinement using the ZZ-estimator and the SPR-C smooth stress field.

weak sense to avoid ill-conditioning of the systems to solve at each SPR patch. The non-conforming nature of the meshes in the cgFEM prevents the direct coupling of SPR patches between bodies in contact. However, the results show that the contact pressure equilibrium is greatly improved with the SPR-C, especially inside those elements completely contained within the contact zone. The use of polynomials to build the recovered stress field prevents to capture the pressure discontinuity that appears at the end of the contact area. Nevertheless, the accuracy of the resulting contact stress distribution is clearly enhanced when the SPR-C technique is considered.

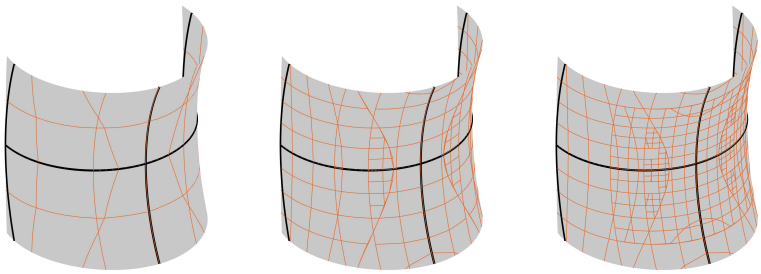

(a) 6840 DOF (b) 15555 DOF (c) 42333 DOF

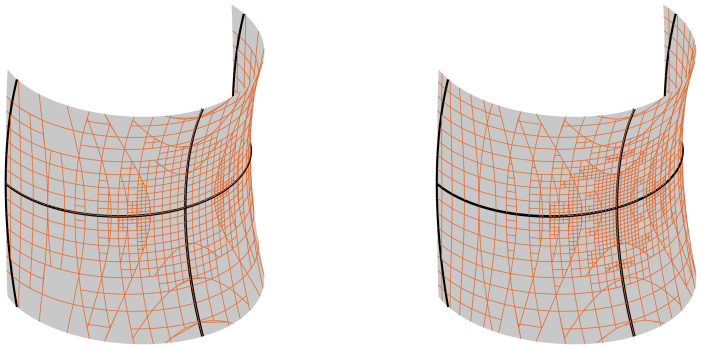

(d) 123306 DOF (e) 223743 DOF

Fig. 16: Example 3. Sequence of five meshes obtained through error-based *h*-adaptive refinement. Detail of the intersection between the discretization mesh and geometry around the contact area.

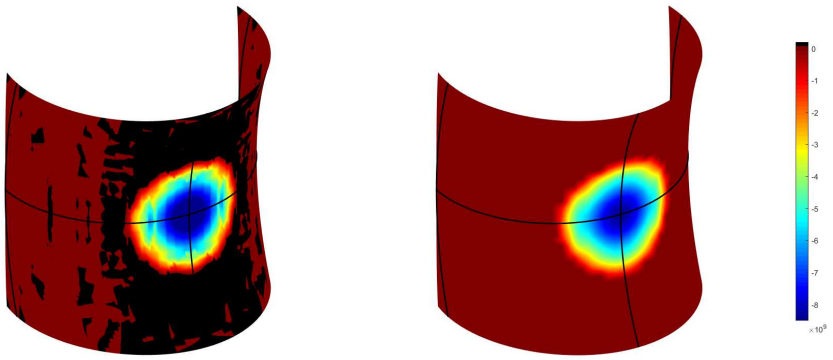

Fig. 17: Example 3. Surface normal tractions $(\mathbf{n}\cdot\boldsymbol{\sigma})\mathbf{n}$ using the FE solution (left) and the smooth stress obtained with the SPR-C (right) for the last *h*-adapted mesh. Negative values represent compression stress. Positive values (physically unfeasible) are colored in black.

The numerical examples show that the definition of the smooth field $\boldsymbol{\sigma}^*$ and the effectivity of the ZZ estimator are clearly improved when including the contact boundary equilibrium in the SPR-C. Finally, we have combined the ZZ estimator with an automatic *h*-adaptive refinement procedure that increases the efficiency of 3D contact problems solution, requiring fewer degrees of freedom to reach a prescribed error level. The *h*-adaptive procedure guided by the accurate recovery-based error estimator is able to locate the limit of the contact area and adequately refine the mesh in these regions, providing a better spatial discretisation to capture the end of the contact zone.

Acknowledgements The authors want to thank Generalitat Valenciana (PROMETEO/2016/007), the Spanish Ministerio de Economa, Industria y Competitividad (DPI2017-89816-R), the Spanish Ministerio de Ciencia, Innovación y Universidades (FPU17/03993) and Universitat Politècnica de València (FPI2015) for the financial support to this work.

References

1. Wriggers P. Computational contact mechanics, second ed., Springer; 2006.
2. Ainsworth M, Oden JT. A Posteriori Error Estimation in Finite Element Analysis. vol. 37. John Wiley & Sons; 2000.
3. Wriggers P, Scherf O. Adaptive finite element techniques for frictional contact problems involving large elastic strains. Computer Methods in Applied Mechanics and Engineering. 1998;151(3-4):593–603.
4. Wriggers P, Scherf O. Different a Posteriori error estimators and indicators for contact problems. Mathematical and Computer Modelling. 1998;28(4-8):437–447.
5. Lee CY, Oden JT. A posteriori error estimation of h-p finite element approximations of frictional contact problems. Computer Methods in Applied Mechanics and Engineering. 1994 mar;113(1-2):11–45.
6. Coorevits P, Hild P, Pelle JP. A posteriori error estimation for unilateral contact with matching and nonmatching meshes. Computer Methods in Applied Mechanics and Engineering. 2000 may;186(1):65–83.
7. Wohlmuth BI. An a Posteriori Error Estimator for Two-Body Contact Problems on Non-Matching Meshes. J Sci Comput. 2007;33:25–45.
8. Kuss F, Lebon F. Error estimation and mesh adaptation for Signorini–Coulomb problems using E-FEM. Computers & Structures. 2011;89(11-12):1148–1154.
9. Zienkiewicz OC, Zhu JZ. A simple error estimator and adaptive procedure for practical engineerng analysis. International Journal for Numerical Methods in Engineering. 1987;24(January 1986):337–357.
10. Zienkiewicz OC, Zhu JZ. The superconvergent patch recovery and a posteriori error estimates. Part 1: The recovery technique. International Journal for Numerical Methods in Engineering. 1992;.
11. Becheur A, Tahakourt A, Coorevits P. An a posteriori error indicator for Coulomb's frictional contact. Mechanics Research Communications. 2008 dec;35(8):562–575.
12. Liu H, Ramière I, Lebon F. On the coupling of local multilevel mesh refinement and ZZ methods for unilateral frictional contact problems in elastostatics. Computer Methods in Applied Mechanics and Engineering. 2017 aug;323:1–26.
13. Nadal E, Ródenas JJ, Albelda J, Tur M, Tarancón JE, Fuenmayor FJ. Efficient Finite Element Methodology Based on Cartesian Grids: Application to Structural Shape Optimization. Abstract and Applied Analysis. 2013 apr;2013:1–19.
14. Marco O, Sevilla R, Zhang Y, Ródenas JJ, Tur M. Exact 3D boundary representation in finite element analysis based on Cartesian grids independent of the geometry. International Journal for Numerical Methods in Engineering. 2015 aug;103(6):445–468.
15. Navarro-Jiménez JM, Tur M, Albelda J, Ródenas JJ. Large deformation frictional contact analysis with immersed boundary method. Computational Mechanics. 2018;62(4):853–870.
16. Marco O, Ródenas JJ, Navarro-Jiménez JM, Tur M. Robust h-adaptive meshing strategy considering exact arbitrary CAD geometries in a Cartesian grid framework. Computers & Structures. 2017;193:87–109.
17. Ródenas JJ, Tur M, Fuenmayor FJ, Vercher A. Improvement of the superconvergent patch recovery technique by the use of constraint equations: The SPR-C technique. International Journal for Numerical Methods in Engineering. 2007;70(October 2006):705–727.
18. Zienkiewicz OC, Zhu JZ. The superconvergent patch recovery (SPR) and adaptive finite element refinement. Computer Methods in Applied Mechanics and Engineering. 1992;101(1):207 – 224.

19. Ródenas JJ, González-Estrada Oa, Díez P, Fuenmayor FJ. Accurate recovery-based upper error bounds for the extended finite element framework. Computer Methods in Applied Mechanics and Engineering. 2010 aug;199(37-40):2607–2621.
20. Nadal Soriano E. Cartesian grid FEM (cgFEM): High performance h-adaptive FE analysis with efficient error control. Application to structural shape optimization. Universitat Politècnica de València. Valencia (Spain); 2014.
21. Blacker T, Belytschko T. Superconvergent patch recovery with equilibrium and conjoint interpolant enhancements. International Journal for Numerical Methods in Engineering. 1994;37(3):517–536.
22. Díez P, José Ródenas J, Zienkiewicz OC. Equilibrated patch recovery error estimates: simple and accurate upper bounds of the error. International Journal for Numerical Methods in Engineering. 2007 mar;69(10):2075–2098.
23. Nadal E, Díez P, Ródenas JJ, Tur M, Fuenmayor FJ. A recovery-explicit error estimator in energy norm for linear elasticity. Computer Methods in Applied Mechanics and Engineering. 2015 apr;287:172–190.
24. Badia S, Verdugo F, Martn AF. The aggregated unfitted finite element method for elliptic problems. Computer Methods in Applied Mechanics and Engineering. 2018;336:533 – 553.
25. Zienkiewicz OC, Zhu JZ, Wu J. Superconvergent patch recovery techniques some further tests. Communications in Numerical Methods in Engineering;9(3):251–258.
26. Fuenmayor FJ, Oliver JL. Criteria to achieve nearly optimal meshes in the h-adaptive finite element mehod. International Journal for Numerical Methods in Engineering. 1996;39(January):4039–4061.
27. Babuška I, Strouboulis T, Upadhyay CS. A model study of the quality of a posteriori error estimators for linear elliptic problems. Error estimation in the interior of patchwise uniform grids of triangles. Computer Methods in Applied Mechanics and Engineering. 1994;114(3):307 – 378.